

# Real-Time Machine Learning Control of a Hall Thruster Discharge Plasma

IEPC-2025-515

*Presented at the 39th International Electric Propulsion Conference  
Imperial College London, London, United Kingdom  
September 14-19, 2025*

Ajay Krishnan<sup>1</sup>, Bogdan Vlahov<sup>2</sup>, Jason Gibson<sup>3</sup>, Dan Lev<sup>4</sup>, Evangelos Theodorou<sup>5</sup>, Mitchell Walker<sup>6</sup>  
and Maryam Saeedifard<sup>7</sup>

*Georgia Institute of Technology, Atlanta, Georgia, 30332, USA*

Facility effects are known to alter Hall thruster performance between ground and space. Furthermore, discharge current oscillations are linked to impacting both the lifetime and thrust of Hall thrusters. In this work, we present a machine learning-based control framework designed for nonlinear, time-varying systems with hysteresis that can mitigate breathing mode oscillations and adapt to environmental changes. Unlike reactive approaches such as PID control, our method is predictive and flexible across a range of control objectives. Specifically, we employ echo state networks (ESNs), a class of recurrent neural networks well-suited for time-series prediction. To train and test the model, we apply a diverse set of discharge voltage perturbations—including sine, triangle, square, ramp, chirp, noise, pseudorandom binary sequence, and PID—on a 6-kW H6 Hall thruster operated at 400 V and 4.3 A, and measure the resulting discharge current as a part of a process known as system identification. Using extended convergent cross mapping, we confirm causal relationships between the applied perturbations and discharge current response. The ESN achieves 90% prediction accuracy on previously unseen time-series data based on variance. We then integrate the ESN into a nonlinear model predictive control (NMPC) framework, creating a machine learning controller, to compute optimal control trajectories that suppress discharge oscillations. NMPC simulations indicate that discharge current oscillations can be reduced by over 90%. Finally, we outline a deployment strategy in which the learned control policy is embedded as a multilayer perceptron on a field-programmable gate array, enabling real-time experimental implementation. The machine learning controller has the potential to be applicable to other operating points by following a standard procedure of system identification and control optimization.

## I. Nomenclature

HPEPL	= High Power Electric Propulsion Laboratory	ODE	= Ordinary Differential Equation
HLS	= High Level Synthesis	PDE	= Partial Differential Equation
PPU	= Power Processing Unit	HET	= Hall Effect Thruster
VTF	= Vacuum Test Facility	MFC	= Mass Flow Controller
BM	= Breathing Mode	FFT	= Fast Fourier Transform

---

<sup>1</sup>Graduate Research Assistant, School of Electrical and Computer Engineering, ajaykrishnan@gatech.edu

<sup>2</sup>Graduate Research Assistant, Institute for Robotics and Intelligent Machines, bvlahov3@gatech.edu

<sup>3</sup>Graduate Research Assistant, Institute for Robotics and Intelligent Machines, jgibson37@gatech.edu

<sup>4</sup>Research Engineer, School of Aerospace Engineering, dan.lev@gatech.edu

<sup>5</sup>Associate Professor, School of Aerospace Engineering, evangelos.theodorou@gatech.edu

<sup>6</sup>Chair, School of Aerospace Engineering, mitchell.walker@coe.gatech.edu

<sup>7</sup>Professor, School of Electrical and Computer Engineering, maryam@ece.gatech.edu

STFT	= Short-Time Fourier Transform	CWT	= Continuous Wavelet Transform
EMD	= Empirical Mode Decomposition	ML	= Machine Learning
NN	= Neural Network	RNN	= Recurrent Neural Network
ESN	= Echo State Network	RMSE	= Root Mean Square Deviation
NRMSE	= Normalized Root Mean Square Error	MLP	= Multilayer Perceptron
PID	= Proportional-Integral-Derivative	DC	= Direct Current
AC	= Alternating Current	ILC	= Iterative Learning Control
NMPC	= Nonlinear Model Predictive Control	IPOPT	= Interior Point Optimizer
SQP	= Sequential Quadratic Programming	AM	= Amplitude Modulation
FM	= Frequency Modulation	PM	= Phase Modulation
eCCM	= Extended Convergent Cross Mapping	EKF	= Extended Kalman Filter
ADC	= Analog-to-Digital Converter	FPGA	= Field-Programmable Gate Array
DAC	= Digital-to-Analog Converter	GPU	= Graphics Processing Unit
CPU	= Central Processing Unit	LSTM	= Long Short-Term Memory
RLS	= Recursive Least Squares	$V_P$	= PPU Voltage
RMS	= Root Mean Square	PP	= Peak-to-Peak
0D	= Zero-Dimensional	EMI	= Electromagnetic Interference
IVB	= Current, Voltage, Magnetic Field	RLC	= Resistor, Inductor, Capacitor
LTI	= Linear Time-Invariant	LTV	= Linear Time-Varying
NLTI	= Nonlinear Time-Invariant	NLTV	= Nonlinear Time-Varying
PRBS	= Pseudorandom Binary Sequence	SNR	= Signal-to-Noise Ratio
$RF$	= Filter Resistance	$CF$	= Filter Capacitance
$RH$	= Harness Resistance	$LH$	= Harness Capacitance
$LH$	= Harness Inductance	$I_D$	= Discharge Current
$VM$	= Modulation Voltage	$e$	= Electron Charge
$A_C$	= Channel Cross-Sectional Area	$M_i$	= Ion Mass
$R_\Delta$	= Channel Width	$\zeta_{ion}$	= Ionization Rate Coefficient
$L_{ch}$	= Channel Length	$N_{int}$	= Injected Neutral Number Density at Anode
$\varepsilon_w$	= Electron Energy Loss to Wall	$\nu_w$	= Electron Wall Collision Frequency
$\chi$	= Ionization Cost	$\varepsilon_{ion}$	= Ionization Energy Loss
$U_{i,w}$	= Ion Acoustic Speed	$E$	= Electric Field
$V_{CF}$	= Filter Capacitor Voltage	$I_{LH}$	= Harness Inductor Current
$N_i$	= Ion Number Density	$N_n$	= Neutral Number Density
$U_i$	= Ion Velocity	$U_e$	= Electron Velocity
$T_e$	= Electron Temperature	$\hat{h}(n)$	= Intermediate Reservoir Neuron Activations
$h(n)$	= Reservoir Neuron Activations	$x(n)$	= Training Input Signal
$y(n)$	= Output	$W_{in}$	= Input Weight Matrix
$W_{out}$	= Output Weight Matrix	$W_{rec}$	= Recurrent Weight Matrix
$W_{fb}$	= Feedback Connections	$b_{rec}$	= Recurrent Bias
$b_{out}$	= Output Bias	$\alpha$	= Leak Rate
$Y_{target}$	= Target Output	$\beta$	= Regularization Term

$I$	= Identity Matrix	$Y_{pred}$	= Predicted Output
$K_P$	= Proportional Gain	$K_I$	= Integral Gain
$K_D$	= Derivative Gain	$V_{AC}$	= AC Voltage Component
$I_{AC}$	= AC Current Component	SSF	= Single-Step Forced

## II. Introduction

A HET is an electrostatic plasma device that produces thrust via the acceleration of ions [1, 2]. Developed in the 1960s, HETs have become increasingly adopted for satellite propulsion due to their mass efficiency compared to chemical propulsion systems [2]. To expand their use in satellites and deep space missions, ongoing advancements aim to improve thrust, specific impulse, efficiency, and thruster lifetime. These developments rely on ground-based testing in dedicated vacuum facilities designed to replicate the space environment as closely as possible. However, space conditions cannot be fully reproduced on the ground, resulting in deviations in measured performance and plasma behavior [3].

Vacuum chambers introduce what are referred to as “facility effects” that change thruster performance on the ground compared to that in space [3–6]. Facility effects occur because ground facility pumping systems cannot reach the low-pressure levels as in space [7]. Additionally, the vacuum chambers are made out of metal, creating current paths that otherwise do not exist in the space environment [3–6]. Lastly, sputtering, originating from the chamber walls back onto and into the thruster, may interfere with the discharge and affect HET lifetime [3]. Understanding and mitigating such facility effects is therefore essential for accurate HET performance characterization.

Discharge current oscillations are another critical factor influencing HET operation [8, 9]. These oscillations originate from plasma instabilities, with the dominant mode being the BM [10]. The BM arises from predator–prey interactions between neutrals and electrons, producing variations in plasma density within the discharge chamber [10]. It can be described using conservation equations for mass, momentum, and energy, which enable modeling of the discharge plasma as an electrical load [11]. Typically occurring in the tens of kHz range, BM oscillations can drive current amplitudes exceeding 100% of the mean [10]. Such oscillatory dynamics degrade thruster performance, contribute to wall erosion, and generate EMI, motivating recent efforts to develop active control strategies [12–15].

HETs are nonlinear, spatially-varying, time-varying, and causal systems that exhibit hysteresis [16, 17]. Plasma diagnostics show spatial dependence, while spatially-averaged data from electrical diagnostics reveal time-varying and hysteretic nature. Nonlinearity of the discharge plasma has been demonstrated by using small-signal linearization to show that discharge impedance is constant for small perturbations but begins to change for larger perturbations [18]. The discharge plasma is, however, LTV and not LTI for smaller perturbations, which can be observed when not using a time constant much longer than the breathing mode period that averages out the time-varying behavior. Analytical techniques for analyzing nonlinear, spatially-varying, and time-varying behavior require the use of algorithms beyond the FFT, which applies only for signals produced by LTI systems. The STFT and CWT may be used for LTV systems, while the EMD and similar methods, such as the IMFogram, may be used for NLTI and NLTV systems [16]. It is important to understand the dynamics of the HET so that applicable control strategies can be applied to handle the dynamics.

While IVB maps can identify operating points where oscillations are lower in amplitude, it is sometimes still necessary to seek to reduce the amplitude even further, and it may even be the case where there is a desire to operate a thruster at a more oscillatory point for performance reasons [19]. A simple case of HET control involves tuning an RLC network placed in the discharge circuit that can be used to reduce oscillations [20, 21]. However, the RLC network cannot be changed at a fast rate and is static. Mass flow rate control can also only be accomplished at slow time scales [22]. Magnetic field control is difficult to achieve in real-time due to the resulting back EMF from changing magnetic fields at a fast rate, and thus it is better to tune to optimal values without or with slow variations [20]. Past research has explored perturbing discharge voltage with PID control and phase synchronization of discharge voltage and discharge current [12, 13, 23]. Due to limitations in using PID for nonlinear time-varying loads such as a HET, some researchers have investigated using ML to control a HET, such as ILC [22, 24]. Existing discharge plasma models are not fully predictive, whereas ML has the potential to outperform these models using data-driven and physics-informed approaches. ML control could potentially leverage various HET power supplies simultaneously to control the HET [22, 25]. Past research has also explored using ESNs for time series prediction of discharge current [17].

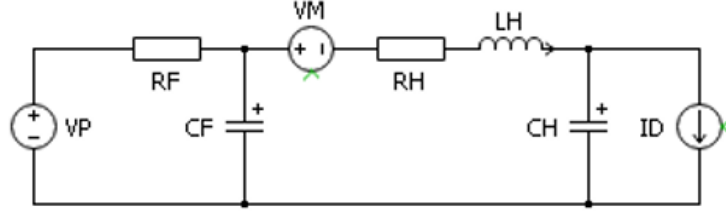
Active control of a HET is desired as it can shape oscillations to reduce wall erosion, reduce EMI, protect the PPU, improve stability, and improve thrust [12–15]. We propose a ML control approach that can be used to make intelligent PPUs. This approach can allow HETs to operate optimally by allowing them to either reduce oscillations or phase

synchronize voltage and current to increase thrust. The approach operates faster than the BM oscillation timescale and uses an NMPC controller on a NN that could potentially update over time. NMPC allows for predictive rather than reactive control and provides flexibility for control objectives as it classically involves solving a nonlinear optimization problem given a dynamics model and constraints. With increasing data availability, NNs can better generalize the dynamics of the HET discharge plasma and aid in computing better control trajectories [26]. ML control could also potentially predict and prevent mode-hopping behavior in HETs, where the HET switches between lower-thrust plume modes and higher-thrust jet modes [27].

### III. Control Problem and Approach

We start by modeling the discharge circuit of the HET and identifying the control problem. We then discuss our active control approach by investigating time and frequency domain behavior that we seek to change. Lastly, we discuss three different ways to control a HET that we argue are best achieved using ML rather than PID. The work presented here is broken into control simulations on a 0D ionization model, experimentation to obtain a HET dataset including PID control, training, testing, and tuning of an ESN using the dataset, PID and NMPC control simulations using the ESN, and deployment onto an FPGA for use in an experiment to demonstrate the ML controller for oscillation reduction.

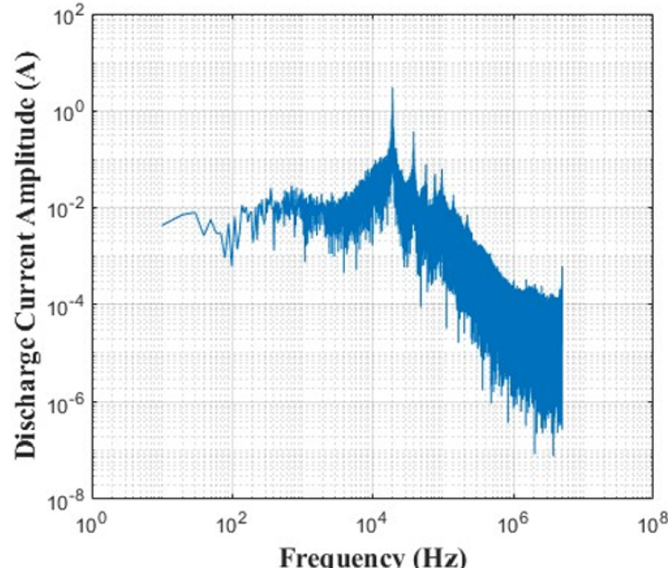
The circuit in Figure 1 consists of a DC voltage source (the PPU output), a RC low-pass discharge filter to protect the PPU from oscillations, a modulation voltage, a harness transmission line model (the source of discharge voltage oscillations via time-varying current flowing through LH), and the load represented by a variable current source [28]. The following control model in Equation 1 shows that there is coupling between discharge current, modulation voltage, and discharge voltage that requires modeling. For minimizing oscillations, the control objective is to find a trajectory where VM opposes the natural oscillations in VD. However, the choice of control voltage is not as simple as negating the discharge voltage, as the discharge voltage changes with the applied control voltage.



**Fig. 1 Discharge Circuit Diagram**

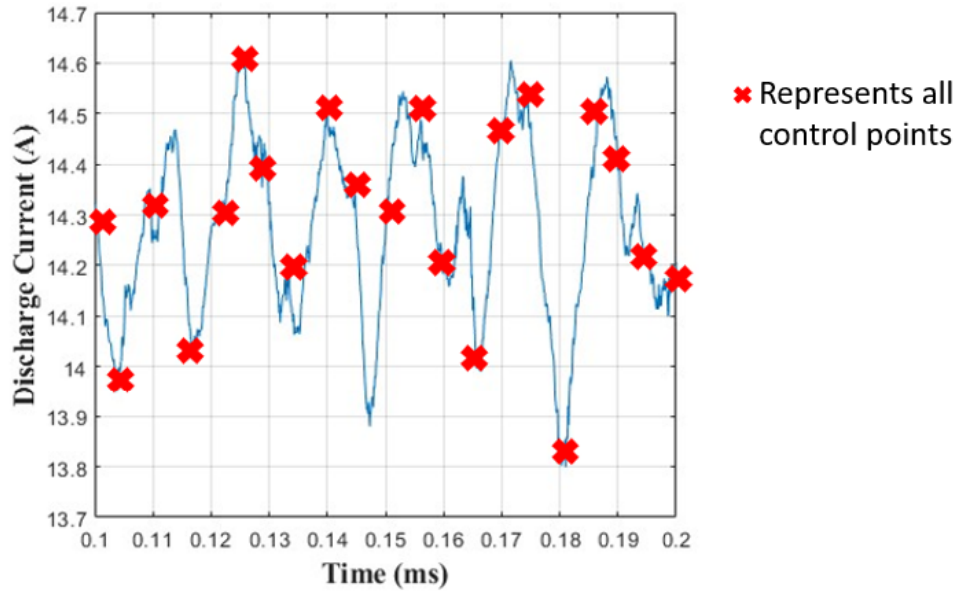
$$V_{CF} - L_H \frac{dI_D}{dt} - V_M - V_D = 0 \quad (1)$$

Figure 2 shows the FFT of the discharge current of the H9 9-kW HET operated at 600 V, 15 A. The FFT at this operating condition reveals a BM peak and harmonics. It is important to note that it is not the case that the breathing mode and harmonics are solely responsible for the oscillations; the sidebands of the peaks also are signals and contribute to the oscillatory behavior. Control does not involve just addressing the peaks, so it is necessary to develop a controller that can handle all oscillations depicted in the FFT. The rationale for control involves active noise cancellation, where waves at various frequencies are canceled by introducing waves that are 180 degrees out of phase, leading to destructive interference [29]. However, in a nonlinear load such as a HET, perturbations at a particular frequency can lead to responses at other frequencies due to frequency coupling, which need to be accounted for.



**Fig. 2 Discharge Current FFT**

Figure 3 shows the philosophy of active control, where the discharge current waveform is shaped through repeated applications of control voltages throughout the BM period. The proper choice of control voltages at the right points in time could allow for oscillation reduction. There are fundamental physical limits on the frequency of the control voltages, due to the behavior of ions, electrons, and neutrals.



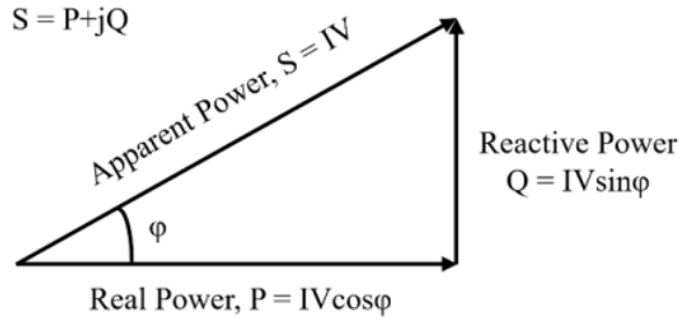
**Fig. 3 Waveform Shaping of HET Discharge Current Oscillations**

Table 1 shows three possible control modes that could be used for a HET. The first is to perturb the discharge voltage to control voltage and current oscillations to reduce wall erosion, reduce EMI, improve stability, and protect the PPU. The second is to perturb the discharge voltage to phase align the discharge voltage and discharge current to increase thrust. The third involves perturbing the discharge voltage to convert discharge current oscillations into AM/FM/PM, as the discharge plasma emits EM waves, which could potentially be used for communications.

**Table 1 Table of Control Modes**

Control Mode	Description
Voltage and Current Oscillation Control	Perturb voltage to control the voltage and current oscillations
Maximum Thrust	Achieved by phase aligning the voltage and current oscillations
AM/FM/PM	Achieved by applying appropriate voltage perturbations that result in AM/FM/PM of discharge current

From an electrical point of view, the approach extends selecting specific RLC components for passive power factor correction to active power factor correction by introducing voltage perturbations. This approach is a drive circuit for HETs. Figure 4 shows that the phase shift between discharge voltage and discharge current dictates the real and reactive power. For maximum thrust and real power, the voltage and current signals should be phase-aligned, minimizing reactive power and maximizing power factor. A 90-degree phase shift results in minimal real power input and, thus, minimal thrust. Rather than minimizing oscillations, it may even be advantageous to increase oscillations while synchronizing discharge voltage and discharge current, or even reduce oscillations while achieving synchronization. It is important to note that while the DC settings of the thruster largely impact thruster performance, the AC behavior also plays a role, and shaping AC behavior can lead to different outcomes in terms of performance.

**Fig. 4 Power Triangle**

In this work, we choose to focus on oscillation reduction before looking into improving thrust or demonstrating AM/FM/PM. The nonlinear optimal control problem for reducing the RMS of the discharge current oscillations is shown as follows, where  $x_k$  represents HET states at time  $k$ ,  $u_k$  represents the control voltage at time  $k$ ,  $f(x_k, u_k)$  represents HET dynamics at HET states and control voltage at time  $k$ ,  $g(x_k, u_k)$  represents the discharge current output at HET states and control voltage at time  $k$ ,  $N$  is the number of steps looking forward,  $j$  represents particular times during the  $N$  steps looking forward,  $\mu$  is the mean discharge current, and  $u_{min}$  and  $u_{max}$  are minimum and maximum bounds on the control voltage:

**Dynamics:**  $x_{k+1} = f(x_k, u_k), \quad i_k = g(x_k, u_k)$

**Objective:** 
$$\min_{\{u_k, \dots, u_{k+N-1}\}} \underbrace{\sum_{j=0}^{N-1} (i_{k+j} - \mu)^2}_{\text{minimize RMS of oscillations}}$$

where  $\mu = \frac{1}{N} \sum_{j=0}^{N-1} i_{k+j}$

**Subject to:**

$$\begin{aligned} x_{k+j+1} &= f(x_{k+j}, u_{k+j}), \quad j = 0, \dots, N-1, \\ u_{\min} &\leq u_{k+j} \leq u_{\max}, \quad j = 0, \dots, N-1, \\ x_k &\text{ given.} \end{aligned}$$

## IV. Methods

Section A discusses how we perform system identification on a HET using voltage perturbations. Section B discusses the ML model we selected for representing the relationship between control voltage and discharge current based on the perturbation response data collected during system identification. Section C explains the experimental setup that we use for collecting perturbation response data and control. Section D explains the PID control experiment that we conducted on the HET load that also is used for creating the ML model based on perturbation responses from applying the PID control. Lastly, Section E discusses how we use the ML model as a part of an NMPC framework in a simulation where optimal control voltages are determined that minimize discharge current oscillations.

### A. System Identification

To control the HET discharge plasma, we must first determine a model for HET discharge plasma dynamics through a process known as system identification, which we can then use to determine control trajectories that allow us to achieve our control objectives. We use an Agilent 33522A function generator as the signal source, an AE Techtron 9110 switch-mode power amplifier, and two AE Techtron T2000 transformers in parallel for isolation, each with primary to secondary turns ratio of two to one, to interface with the discharge circuit for load perturbation, shown in Figure 5. The power amplifier and transformer each have a bandwidth of 250 kHz. Each transformer is rated for 500 W, allowing up to 1 kW to be added to the plasma. The power amplifier is responsible for amplifying the voltage of the input signal while also increasing its current. DC offset cancellation is included since DC will saturate the transformer, the difference amplifier is included to boost the signal to the highest allowable level of the power amplifier, and the bandpass filter is used to limit the injection signal frequency between the cutoff of the discharge filter and the power amplifier and transformer bandwidth. This setup effectively places a variable voltage source in series with the HET. The system can handle the plasma inrush current and fault conditions. PPU output voltage changes are limited by the discharge filter, so the injection path needs to be placed after the filter to enable perturbation and control at higher frequencies and fast time scales. However, for control at slow time scales, as in the case of the ILC approach, the PPU output voltage can be changed without attenuation from the discharge filter [22]. Control at faster time scales has added complexity but has the potential to be more effective.

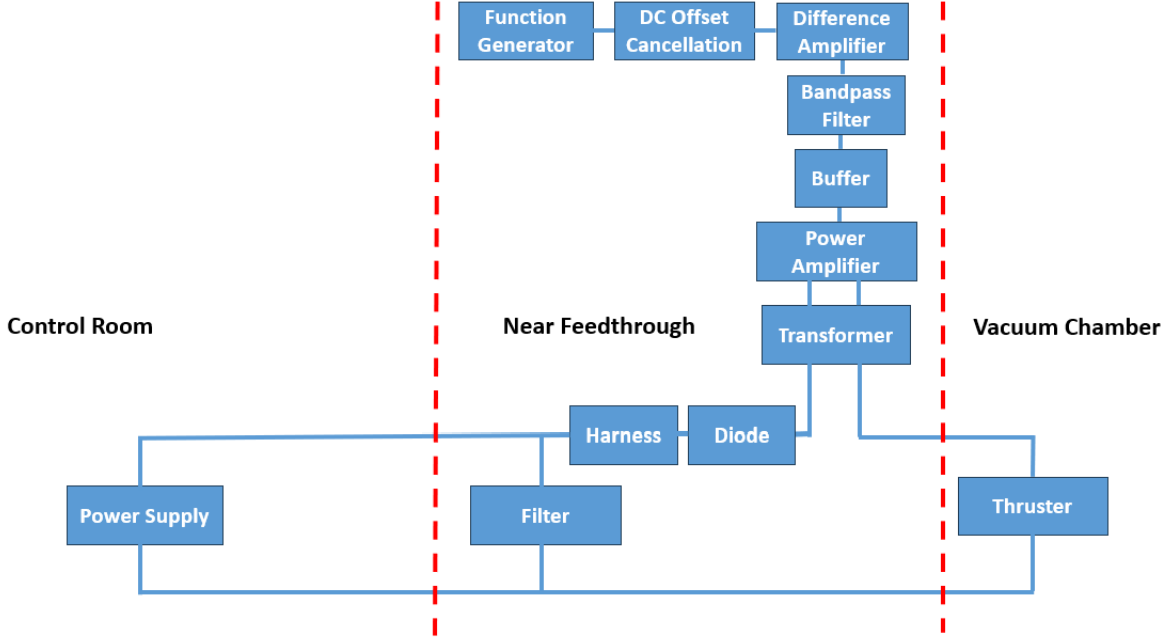


**Fig. 5 Load Characterization Experiment Diagram**

The perturbations we add to the discharge to assist with system identification of the discharge plasma are summarized in Table 2. These include sine waves for basic characterization of the plasma response, square waves to capture nonlinear responses, triangle waves which capture elements of both sine and square waves, ramp as a blend between triangle and square waves, chirps for characterizing time-varying effects, combinations of sinusoids to capture coupling, noise to capture stochastic effects, and lastly PRBS. These perturbations are applied at various amplitudes up to 2.5 V, frequencies between 7 kHz and 19 kHz, and phases. This process can be applied to any HET operating point to learn the dynamics and create a ML controller. The system identification approach is still applicable for operating points that exhibit mode-hopping behavior.

**Table 2 Load Characterization Test Matrix**

Waveform Perturbation Type (Various Amplitudes, Frequencies, and Phases)
Sine
Triangle
Square
Ramp
Chirp
Discharge Voltage (Combination of Sinusoids)
Noise
PRBS
PID

## B. ML Model

The main motivation for constructing an ML model is because HET discharge plasma models are not predictive enough to allow for control on their own. ML allows us to use a data-driven approach and additionally a physics-informed approach if desired to model HET discharge plasma dynamics. ML models are intended to predict the deterministic parts of the discharge plasma while attempting to predict the random contributions from plasma turbulence. In constructing a



ML model of the discharge plasma, it is necessary to measure the underlying states governing the plasma, specifically their response to perturbations. These include electrical states in the discharge circuit using the perturbation approach discussed previously along with plasma states. Plasma diagnostics are used to measure the plasma states shown in Table 3 below. However, it is difficult to measure the plasma states in real-time in the discharge. Non-intrusive plasma diagnostics would have to be used so that the plasma is not perturbed from an additional boundary condition.

**Table 3 Time Scales of Various Plasma Diagnostics**

Plasma Diagnostic	Invasive?	Plasma Parameter	Time Scale
Faraday Probe	Yes	$U_i, N_i$	Microseconds
Laser Induced Fluorescence	No	$U_i, N_i$	Not Real-Time
Triple Langmuir Probe	Yes	$T_e, N_i$	Microseconds
Laser Thomson Scattering	No	$T_e, U_e, N_i$	Not Real-Time
Optical Emission Spectroscopy	No	$T_e, N_n, N_i$	Not Real-Time

It is also difficult to use a 3D plasma discharge model governed by PDEs and take 3D measurements for plasma state estimation using an EKF due to the complexity and time involved in solving the PDE system and obtaining an adequate dataset. 3D control would also require placing electrodes in various spatial locations around the discharge channel. Controlling these electrodes would pose a computational challenge. A more feasible approach would be to use a 0D model, discussed in the Appendix, and take time-varying and spatially-averaged electrical measurements. Physics-informed ML could involve learning the residuals between measurements and predictions from the physics model, and the prediction of these residuals could then be used for control. These residuals would be the unmodeled terms in the 0D ionization model, primarily anomalous electron transport. Others have looked into symbolic regression for determining the physical representation of unmodeled terms not captured in physical models for the discharge plasma, but this procedure is very computationally and time-intensive, thus NNs may be the better option for control applications [30]. However, tuning the EKF can be cumbersome and requires that the plasma state estimate be correct in order to achieve a proper predictive model. Thus, we opt not to use state estimation and stick with just electrical measurements. Furthermore, we use only the mapping between the control voltage and the discharge current for simplicity, though the other electrical states, such as discharge voltage, harness inductor current, and discharge filter capacitor voltage may contribute additional information that may further improve prediction accuracy. A ML model was built using an ESN, which is a form of reservoir computing and a type of RNN that excels at predicting nonlinear and nonstationary time series [31, 32]. The ESN consists of an input layer, a reservoir layer that uses random, fixed recurrent connections that are never trained, and an output layer that is trained using linear regression, and is represented by Equations 2-7 as follows:

$$\hat{h}(n) = \tanh(W_{in}x(n) + W_{rec}h(n-1) + W_{fb}y(n-1) + b_{rec}) \quad (2)$$

$$h(n) = (1 - \alpha)x(n-1) + \alpha\hat{h}(n) \quad (3)$$

$$y(n) = W_{out}h(n) + b_{out} \quad (4)$$

Ridge regression through Tikhonov regularization can be used to determine  $W^{out}$ :

$$Y_{target} = W_{out}X \quad (5)$$

$$W_{out} = Y_{target}X^T(XX^T + \beta I)^{-1} \quad (6)$$

Prediction is accomplished using  $W_{out}^T$ :

$$Y_{pred} = XW_{out}^T \quad (7)$$

The mapping between control voltage and discharge current can be used to determine sequences of control voltages that can minimize discharge current oscillations, shown in Figure 6. Measurements of discharge current can be directly fed into the ESN to make control voltage predictions. We pick ESNs over LSTMs as they can be trained, tested, and tuned much faster on CPUs without the need for GPUs while maintaining comparable prediction accuracy. LSTMs have the potential to be better at learning temporal dependencies, but are more complex than ESNs [31]. ESN stability can also be controlled more easily than MLPs and LSTMs [33].



**Fig. 6 ESN Model of Control Voltage and Discharge Current**

Given the diverse set of perturbations applied to create the training dataset, the ESN can better learn signal from noise since the noise is smoothened. A lock-in amplifier could also potentially be used to improve the SNR of the measurements. Due to the presence of noise, the true discharge current measurements actually look different from what one may observe on an oscilloscope. It is important to control signal rather than noise, and the effectiveness of the control is reduced when more noise is present. Higher power operating points at higher voltages and currents tend to have higher amplitude components with higher SNR, which further improves control performance, also taking into account that higher power generally leads to more erosion and larger oscillations that can be synchronized for increased thrust [15].

### C. Experimental

Experimentation to obtain a perturbation dataset for developing ML control was performed in VTF-2 at the Georgia Institute of Technology High-Power Electric Propulsion Laboratory. An photograph of this facility is shown in Figure 7b. VTF-2 is a stainless-steel chamber measuring 9.2 m in length and 4.9 m in diameter. VTF-2 is evacuated to a rough vacuum using a 495 CFM rotary-vane pump and a 3800 CFM blower. High vacuum is achieved using ten liquid nitrogen-cooled CVI TMI re-entrant cryopumps at a pumping speed of 350,000 l/s on xenon. The cryopump shrouds are fed using the Stirling Cryogenics SPC-8 RL special closed-loop nitrogen liquefaction system [34].

For this study, we used the H6 HET, shown in Figure 7a, a 6-kW class HET developed in partnership between the NASA Jet Propulsion Laboratory, the University of Michigan, and the Air Force Research Laboratory [1]. The H6 employs a centrally mounted LaB<sub>6</sub> cathode. The thruster body and cathode were isolated from facility ground and were electrically floating.

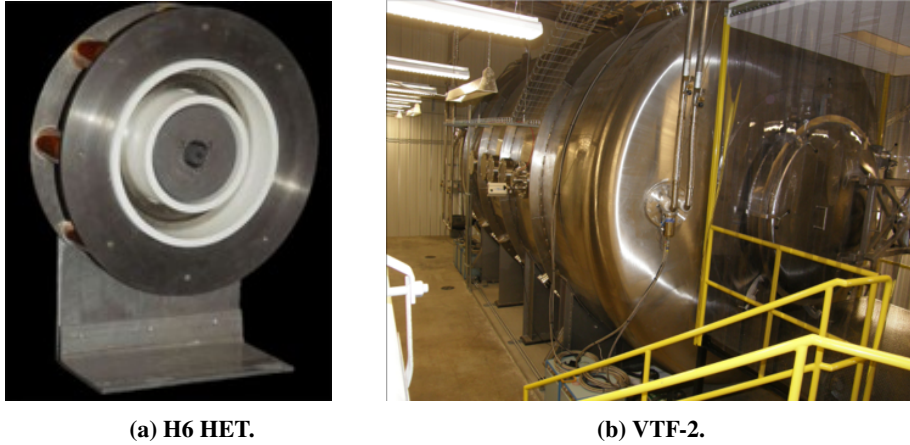


**Fig. 7 Test Article and Facility**

The H6 discharge plasma was controlled using a Magna-Power TS800-24 power supply. All other thruster components were powered using TDK-Lambda GEN80-42 power supplies. A TDK-Lambda GEN600-2.6 and GEN60-25 were used for the cathode keeper and heater, respectively. To protect against HET oscillations, the discharge supply was connected to a RC low-pass discharge filter consisting of a series 0.533-Ohm resistor and a shunt 100-μF capacitor to attenuate discharge current oscillations that are greater than 3 kHz in frequency.

High-purity (99.999%) krypton propellant was supplied to the anode and cathode lines using stainless-steel lines metered with MKS GE50A MFCs. The MFCs were calibrated by measuring the flow upstream of the thruster with

a MesaLabs DryCal 800-10 volumetric flow meter. The uncertainty for anode and cathode line flow is 2% and 5%, respectively.

The power supply voltage, anode and cathode flow rate, and the magnetic field were kept constant during testing. The H6 thruster was operated at one 400 V, 4.3 A thruster operating point, as shown in Table 4. Upon ignition, the H6 thruster was run for three hours until its oscillations became steady after outgassing. The base facility pressure was 10 nTorr, and the facility pressure during operation was 2  $\mu$ Torr.

**Table 4 H6 Thruster Operating Conditions (Krypton)**

Discharge Voltage (V)	Discharge Current (A)	Anode Flow Rate (sccm, mg/s)	Cathode Flow Rate (sccm, mg/s)	Inner Coil Current (A)	Outer Coil Current (A)	Breathing Mode Frequency (kHz)
400	4.3	65, 4.05	6.5, 0.405	2.15	1.96	13

The AC component of the discharge current of the H6 thruster was recorded using a Pearson 110A current monitor placed inside VTF-2, and the control voltage was measured using a BNC cable connected to a HDO6104 Teledyne LeCroy oscilloscope. The uncertainty and bandwidth of the current probe are  $\pm 1\%$  and 20 MHz; for the oscilloscope, they are  $\pm 0.5\%$  full scale and 1 GHz. The oscilloscope has 12 bits of resolution with a selected 25 MS/s sampling rate and is used over an interval of 10 ms for 250,000 samples in all. MATLAB instrument control toolbox with USB and Ethernet for remote desktop of the oscilloscopes were used for semi-automated data collection. HET measurements were collected after it was observed that the peak-to-peak current values had stopped changing within  $\pm 1\%$  variation, taking approximately two hours after ignition due to outgassing.

Systematic and random errors were quantified as part of this study's error analysis. Systematic errors are introduced by voltage and current probes, along with the oscilloscope. Other errors and nonidealities arise from function generator, microcontroller, ADC, FPGA, DAC, power amplifier, transformer, and harness settings.

#### D. PID Control Experiment

As a part of determining perturbation responses, we conducted PID control of the HET discharge plasma. The premise behind PID is that the discharge current oscillations can be reduced by minimizing the error between current measurements and a reference. This is achieved by supplying the error into the PID network, which computes the control voltages needed to accomplish the minimization of the error, represented in Equation 8.

$$V_{AC} = K_P I_{AC} + K_I \int_0^t I_{AC} dt + K_D \frac{dI_{AC}}{dt} \quad (8)$$

The control scheme works by applying voltage at 10 microsecond steps while taking into account propagation and computation delays, shown in Figure 8. For the control approach to be effective, propagation delays between the current probe and the DAC along with computation delays must be minimized.

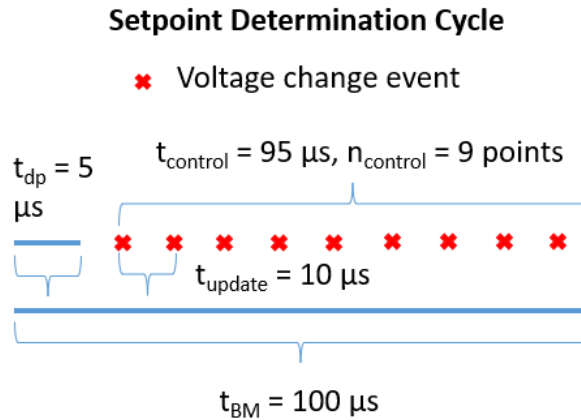


**Fig. 8 Setpoint Timing**



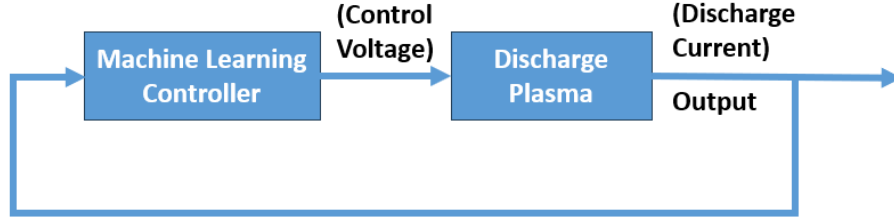


**Fig. 10 ML Control Feedback Diagram**

## V. Results and Discussion

In our work, we seek to compare the performance of NMPC-based ML control approach with PID. We present PID simulation results using a 0D model as the plant, though we are unable to use NMPC on the 0D model due to the stiffness of the model. We present results and discuss oscillation reduction achieved using PID control versus without using PID control. We show that the perturbations actually cause changes in the discharge current using the eCCM algorithm. We show plasma state estimate oscillations using an extended Kalman filter and discuss the resulting plasma physics from PID control beyond electrical changes. We then show the results from ESN training and testing that demonstrate that ESNs can represent discharge current dynamics of a HET. We lastly show that PID and NMPC can control the discharge current oscillations in simulation using the ESN.

### A. 0D Model PID Simulation Results

To start the control work, we ran simulations in MATLAB using the 0D model with the ode23tb stiff solver. Figure 11 shows the discharge current with oscillations of  $20 A_{PP}$ . The breathing mode frequency is 19.7 kHz.

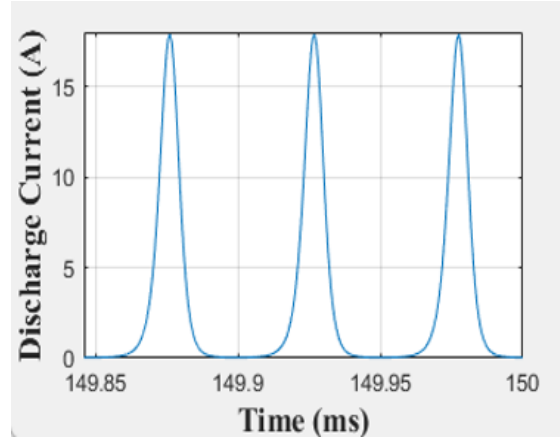
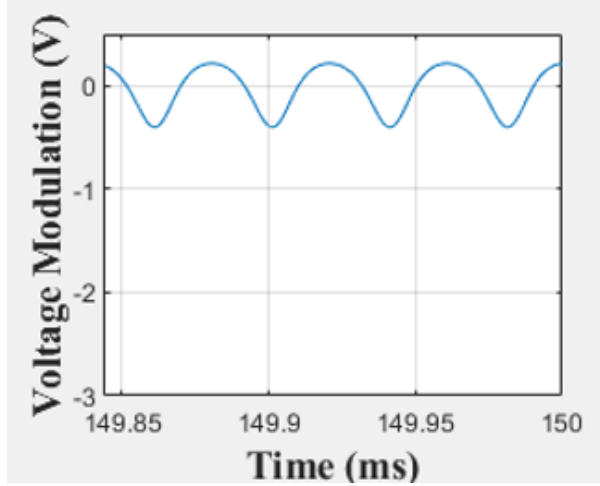
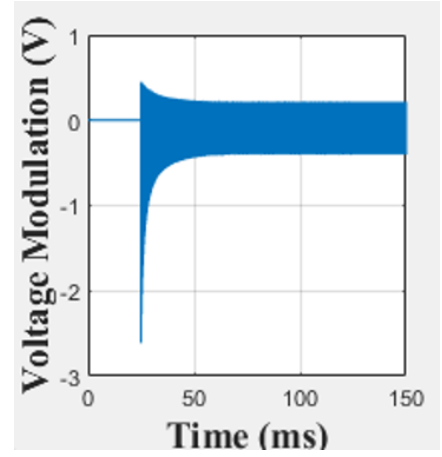


**Fig. 11 0D Model Discharge Current Waveform**

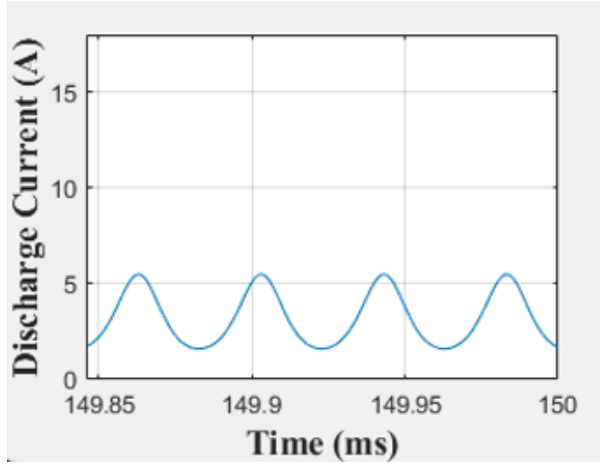
We then ran PID simulations on the 0D model. Figure 12a shows the steady state applied control voltage ranging between -0.5 V and 0.25 V and Figure 12b shows the resulting steady state discharge current with  $2.5 A_{PP}$ , a 87.5% reduction. The discharge current is phase-shifted from the control voltage by 180 degrees. Figures 12c and 12d show the transients of the control voltage being applied along with the resulting discharge current. The control voltage ranges between -2.5 V and 0.5 V until it settles to steady state. A larger control voltage swing is needed to reduce the discharge current oscillation.



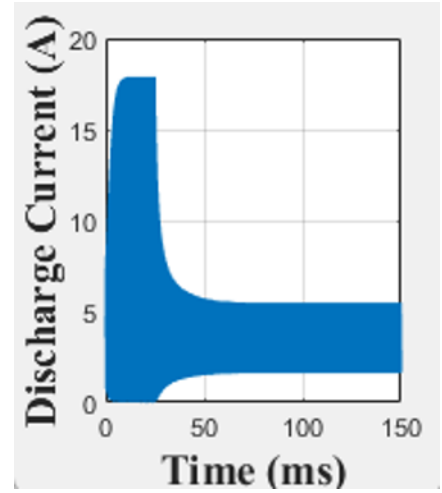
(a) Modulation Voltage Steady State



(b) Modulation Voltage Transition



(c) Discharge Current Steady State



(d) Discharge Current Transition

**Fig. 12 0D Model PID Control Simulation Results**

## B. PID Experiment Results

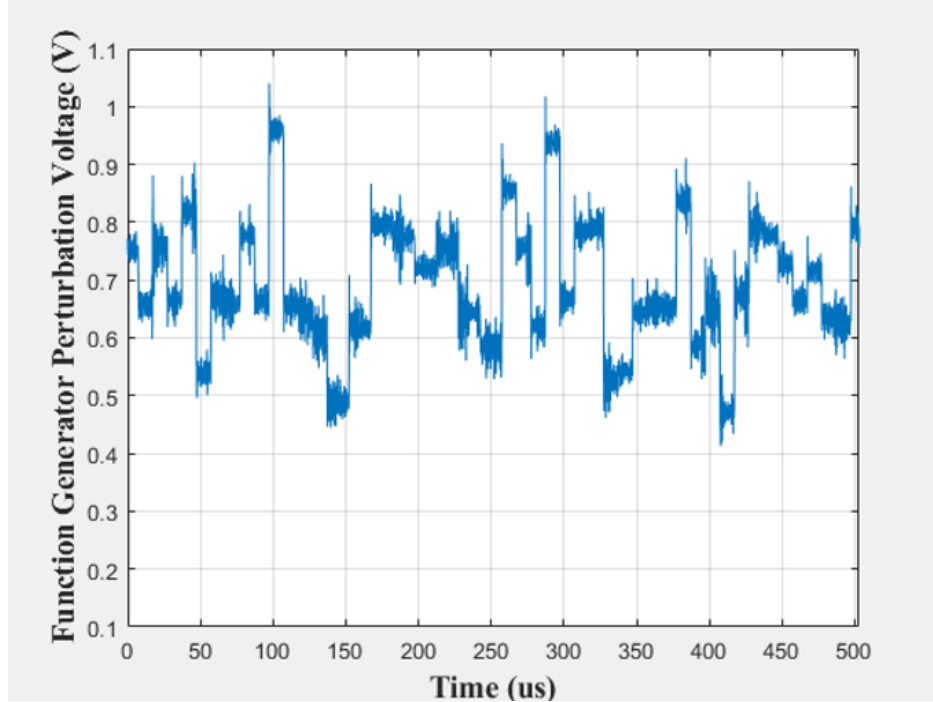
Table 5 shows the  $K_p$  and  $K_d$  values that were used during PID control of the HET discharge plasma. The integral coefficient was not used to keep the control simple and prevent integral windup. It can be observed that increasing the  $K_p$  value improves oscillation reduction, whereas increasing the  $K_d$  value makes the discharge voltage and discharge current more oscillatory. A  $K_p$  value of  $1 \times 10^{-1}$  and a  $K_d$  value of  $1 \times 10^{-9}$  minimizes the discharge current oscillations at 0.578 Arms, a 8.89% reduction, while also reducing the discharge voltage oscillations by 1.19% to 6.819  $V_{RMS}$ . At worst, a  $K_p$  value of  $5 \times 10^{-2}$  and a  $K_d$  value of  $5 \times 10^{-3}$  maximizes the discharge current oscillations at 0.745  $A_{RMS}$ , a 17.42% increases, while also increasing the discharge voltage oscillations by 58.02% to 10.908  $V_{RMS}$ .

**Table 5 PID Characterization**

$K_p$	$K_d$	Discharge Current Oscillation RMS (No Control) (A)	Discharge Current Oscillation RMS (PID Control) (A)	Discharge Current RMS Change (%)	Discharge Voltage Oscillation RMS (No Control) (V)	Discharge Voltage Oscillation RMS (PID Control) (V)	Discharge Voltage RMS Change (%)
$5 \times 10^{-2}$	$1 \times 10^{-9}$	$0.635 \pm 0.034$	$0.635 \pm 0.064$	$0.5 \pm 11.4$	$6.902 \pm 0.193$	$6.676 \pm 0.059$	$-3.24 \pm 2.84$
$5 \times 10^{-2}$	$1 \times 10^{-6}$	$0.635 \pm 0.034$	$0.622 \pm 0.031$	$-1.81 \pm 5.8$	$6.902 \pm 0.193$	$6.695 \pm 0.063$	$-2.94 \pm 3.05$
$5 \times 10^{-2}$	$5 \times 10^{-3}$	$0.635 \pm 0.034$	$0.743 \pm 0.07$	$17.42 \pm 1.66$	$6.902 \pm 0.193$	$10.9047 \pm 0.292$	$58.02 \pm 4.37$
$1 \times 10^{-1}$	$1 \times 10^{-9}$	$0.635 \pm 0.034$	$0.5783 \pm 0.03$	$-8.89 \pm 5.45$	$6.902 \pm 0.193$	$6.819 \pm 0.142$	$-1.19 \pm 2.21$

Figure 13 shows the control voltages determined by the PID controller based on discharge current measurements at a  $K_p$  value of  $1 \times 10^{-1}$  and a  $K_d$  value of  $1 \times 10^{-9}$ , and hereafter we discuss PID performance at these PID gains. It shows a series of different levels of voltage at each  $10 \mu s$  period, representing the 100 kHz loop speed. It is evident that the controller is making control voltage choices during each period of the breathing mode.

Due to the two parallel transformers used in the voltage perturbation approach, the control current required is the same as the discharge current. Reducing the discharge current oscillations reduces the required control current. We can compute the input power required to achieve a discharge current oscillation reduction of approximately 9% by taking the product of the RMS of the injected control voltage and the RMS of the discharge current. By scaling the control voltage by the gain introduced by the perturbation pathway, the RMS voltage at the output of the power amplifier is 12.221 V, while the RMS control current is 0.578 A, yielding a RMS control power of 7.064 W. Out of the 1.72 kW of DC power supplied to the HET, only 0.411% is needed to reduce discharge current oscillations by 9%, through proper selection of perturbation amplitudes and phases at each frequency.

**Fig. 13 PID Control Voltage**

Determining correlation and causality between two signals in a nonlinear and time-varying system, such as a HET, can be accomplished using eCCM, a technique based on Takens' Theorem, and using shadow manifolds [37]. Shadow manifolds are the result of projecting a system's signals onto coordinate axes that are time-lagged. The basis is that if a signal causes another signal, then the signal is recorded in the other signal. To prove that the control voltage (X) is actually acting on the discharge current (Y), we ran an eCCM simulation and obtained the result shown in Figure 14.

This plot shows three identifiable pairs of peaks. The orange peaks represent the discharge current causing the control voltage while the blue peaks represent the control voltage causing the discharge current. Since the first and highest orange curve peak occurs at positive time shifts, this means that discharge current strongly causes the control voltage. This makes sense as the PID algorithm directly computes setpoints based on discharge current measurements. There is a second pair of peaks after the first pair, where the order of the peaks is reversed, and where the second blue peak occurs at positive time shifts. This indicates that there is a weaker causality between control voltage and discharge current. Similarly, the third pair of peaks shows that discharge current causes control voltage. In summary, this scenario occurs where oscillation reduction is smaller.

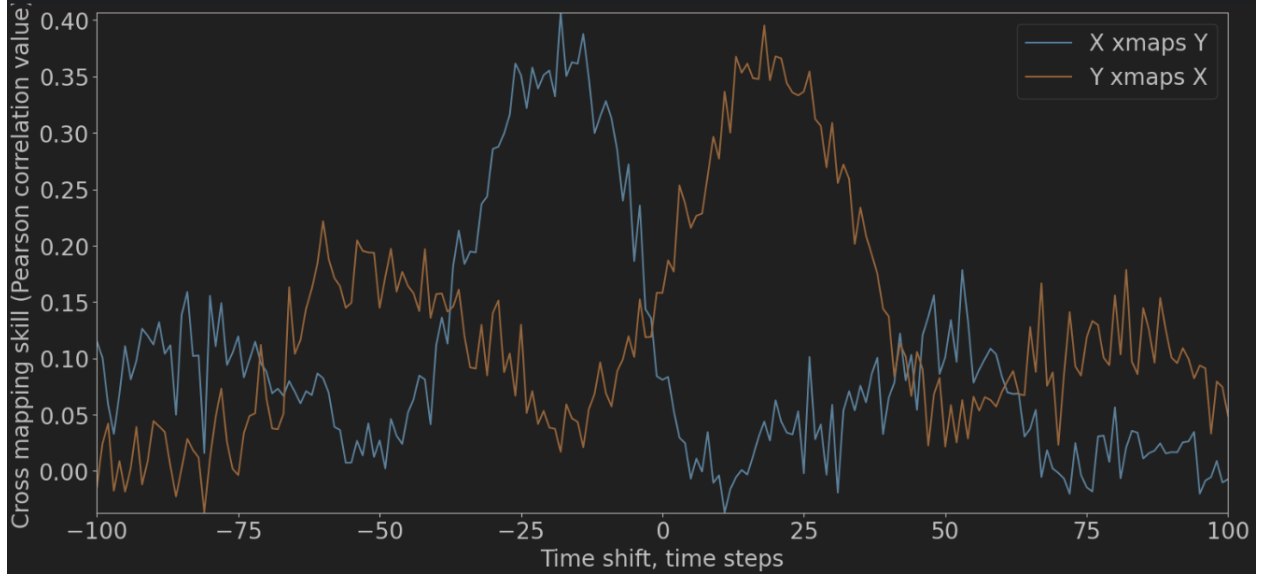
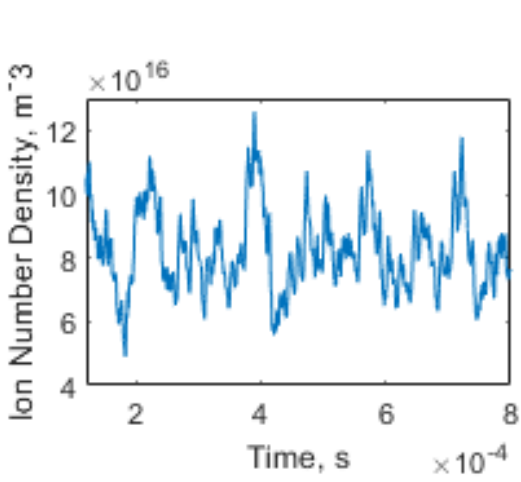


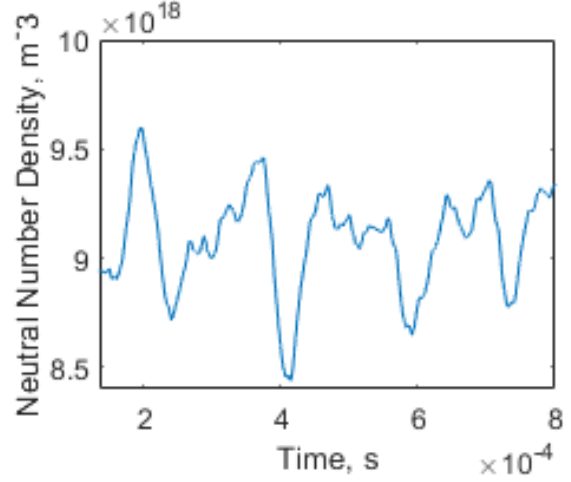
**Fig. 14 eCCM Correlation and Causation of Control Voltage (X) and Discharge Current (Y)**

EKF state estimation was used to estimate the plasma states using the discharge current measurements obtained from the PID experiment. EKF uses the 0D model presented in the Appendix and linearizes the nonlinear dynamics while predicting and correcting using the measurements [11]. In Figures 15-17, we can see that the ion number density, ion velocity, and electron temperature have major peaks and troughs that are in phase, whereas the neutral number density and electron velocity have peaks and troughs that are 180 degrees out of phase. This finding makes sense physically, as ion and neutral populations reach their maximum and minimum at the same time by way of the predator-prey interaction. The electron temperature also contributes to ionization; thus, it makes sense that the ion number density reaches a maximum when the electron temperature reaches a maximum. The ion velocity is also consistent with the ion number density, with a small ion transit time. The electron velocity and neutral number density are in phase since, as the neutral number density increases, more electrons are needed for ionization.



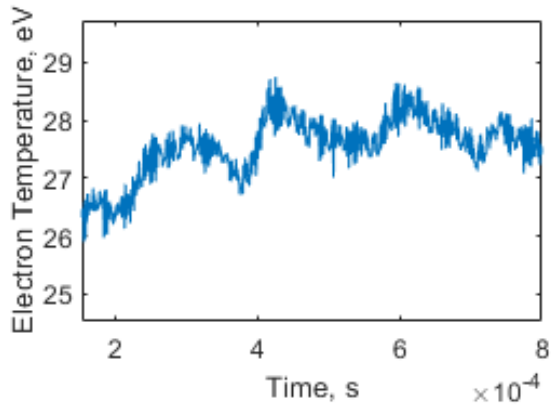


(a) Ion Number Density Estimates

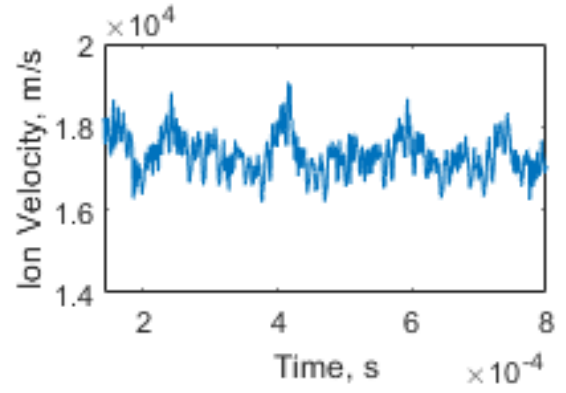


(b) Neutral Number Density Estimates

**Fig. 15 PID EKF Plasma State Estimates (Ion and Neutral Number Densities)**



(a) Electron Temperature Estimates



(b) Ion Velocity Estimates

**Fig. 16 PID EKF Plasma State Estimates (Electron Temperature and Ion Velocity)**

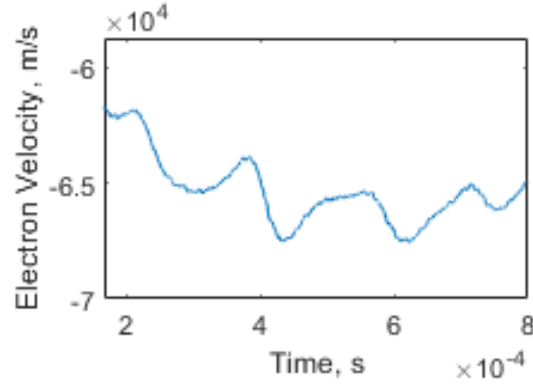


**Fig. 17 PID EKF Plasma State Estimate for Electron Velocity**

Table 6 shows the RMS of the plasma parameters with and without PID control. The reduced discharge current oscillations from using PID result in lower plasma parameter oscillations. The ion number density oscillations decrease by 7.48%, however, the electron velocity oscillations increase by 4.44%. It is possible PID excited higher frequency electron dynamics based on the fact that electrons respond almost immediately to perturbations.

**Table 6 PID Plasma State Estimates**

Plasma Parameter	Oscillation RMS (No Control)	Oscillation RMS (PID)	Oscillation RMS (% Change)
$N_i$	$1.176 \times 10^{16} \pm 8.124 \times 10^{12} \text{ m}^{-3}$	$1.088 \times 10^{16} \pm 7.438 \times 10^{12} \text{ m}^{-3}$	$-7.48 \pm 0.07$
$N_n$	$2.185 \times 10^{17} \pm 2.427 \times 10^{13} \text{ m}^{-3}$	$2.038 \times 10^{17} \pm 2.194 \times 10^{13} \text{ m}^{-3}$	$-6.74 \pm 0.12$
$T_e$	$0.5473 \pm 9.599 \times 10^{-5} \text{ eV}$	$0.508 \pm 8.692 \times 10^{-5} \text{ eV}$	$-7.17 \pm 1.95$
$U_i$	$429.206 \pm 0.514 \text{ m/s}$	$413.5 \pm 0.484 \text{ m/s}$	$-3.66 \pm 0.16$
$U_e$	$2.074 \times 10^3 \pm 0.145 \text{ m/s}$	$2.166 \times 10^3 \pm 0.136 \text{ m/s}$	$4.44 \pm 0.41$

### C. ESN Training and Testing Results

Using a dataset of 180 perturbation conditions consisting of control voltage and discharge current time series, we trained and tested an ESN using a single-step approach and k-fold validation with a Huber loss function. Single-step uses ground-truth data from measurements for predicting the next step, known as teacher-forced training, whereas multi-step predicts over several steps using measurements from one step. We choose single-step over multi-step for simplicity with shorter horizons in NMPC to reduce compounding error. We allow the ESN to washout before training where we eliminate the influence of the ESN’s initial random state, allowing it to warm up and settle. Optuna, a Bayesian optimization framework, was used to tune the hyperparameters of the ESN within a search range, shown in Table 7, which includes the spectral radius, leak rate, sparsity, ridge alpha, reservoir size, Eta0, input scale, and feedback scale [38]. The training, testing, and tuning process took approximately one hour to complete.

**Table 7 ESN Hyperparameters**

Hyperparameter	Description	Search Range	Optimal Value
Reservoir Size	Number of neurons in the reservoir. Larger reservoirs capture temporal dependencies and nonlinearity better but if too large, then increase in computation time and risk of overfitting	[512, 1024]	960 (High)
Spectral Radius	Largest absolute eigenvalue of internal reservoir weight matrix. Controls temporal dependencies, memory strength, and stability	[0.35, 0.95]	0.877 (High)
Leak Rate	Update speed of reservoir states. Governs how fast reservoir neurons update relative to input signal	[0.1, 0.8]	0.724 (High)
Sparsity	Reservoir connectivity. Fraction of zero connections in the reservoir weight matrix	[0.988, 0.997]	0.991 (High)
Ridge Alpha	Output regularization. For ridge regression when training output weight matrix, smaller value means better fitting of data	$[1 \times 10^{-4}, 5 \times 10^{-2}]$	$3.64 \times 10^{-4}$ (Low)
Eta0	Initial learning rate. The step size for iterative solvers when updating weights. Larger value means faster convergence	$[8 \times 10^{-4}, 4 \times 10^{-3}]$	$2.77 \times 10^{-3}$ (High)
Input Scale	Input weight scaling. Scaling factor for weights from inputs to reservoir neurons. Lower value prevents input saturation	[0.3, 5.0]	1.358 (Low)
Feedback Scale	Feedback and memory strength. Scaling factor for feedback weights connecting outputs back to reservoir	[0.3, 3.0]	2.5 (High)

The  $R^2$  value was 0.902, suggesting a strong fit by variance to the dataset, while the RMSE was 0.1917, also suggesting lower error. However, the NRMSE was 0.3122, an acceptable result but suggests that the ESN predicts the dynamics well overall, but doesn’t fully capture the amplitude of the time series. This may indicate a possible limitation

in modeling HET time series data due to its NLTV and hysteretic nature. In Figure 18, we observe excellent agreement in predicting the discharge current when no control is applied for the 8-ms duration signal, with slight under prediction on some peaks.

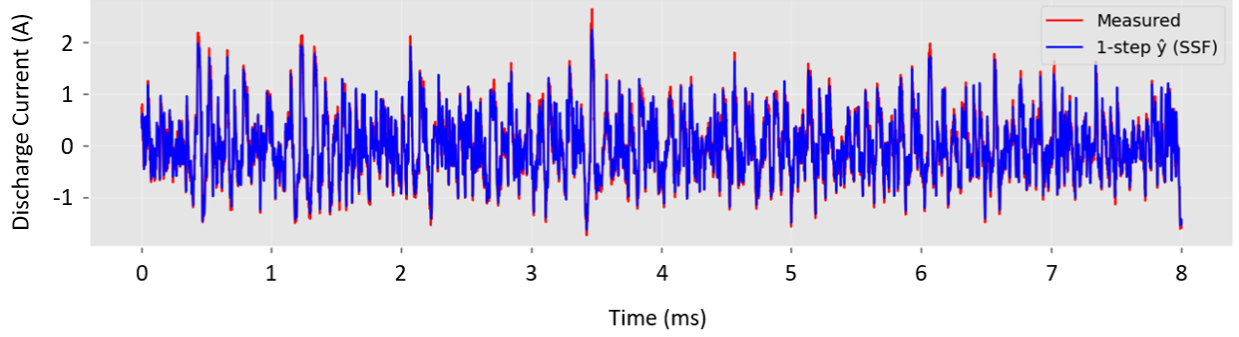


**Fig. 18 Time Series Validation**

#### D. ESN Model PID Simulation Results

In Figure 19, we see how PID affects the discharge current in an ESN simulation at a  $K_p$  value of 5 and a  $K_d$  value of 0.01, taking a few seconds to complete. We use the history of discharge current at no control to initialize the ESN, then apply PID on the ESN to minimize discharge current oscillations. We can see that the oscillations are reduced within 60 microseconds of applying controls. Figure 19d shows the chosen control values at each 10 microsecond step. The PP of the discharge current oscillations reduces from 3  $A_{PP}$  to 0.2  $A_{PP}$ , which is a 93.333% reduction. The control voltage ranges from -0.3 V to 0.6 V, with a close to zero mean since the injection path only takes AC signals. Accounting for gains from the amplifiers between the DAC output to the secondaries of the transformers, the perturbation voltage that would arrive at the HET ranges between -5.625 V and 11.25 V, which is 16.875  $V_{PP}$ . Since the controlled oscillations do not match between PID experiment and PID simulation of an ESN, it is likely that the ESN has not yet fully learned the HET dynamics and that more learning iterations are needed.

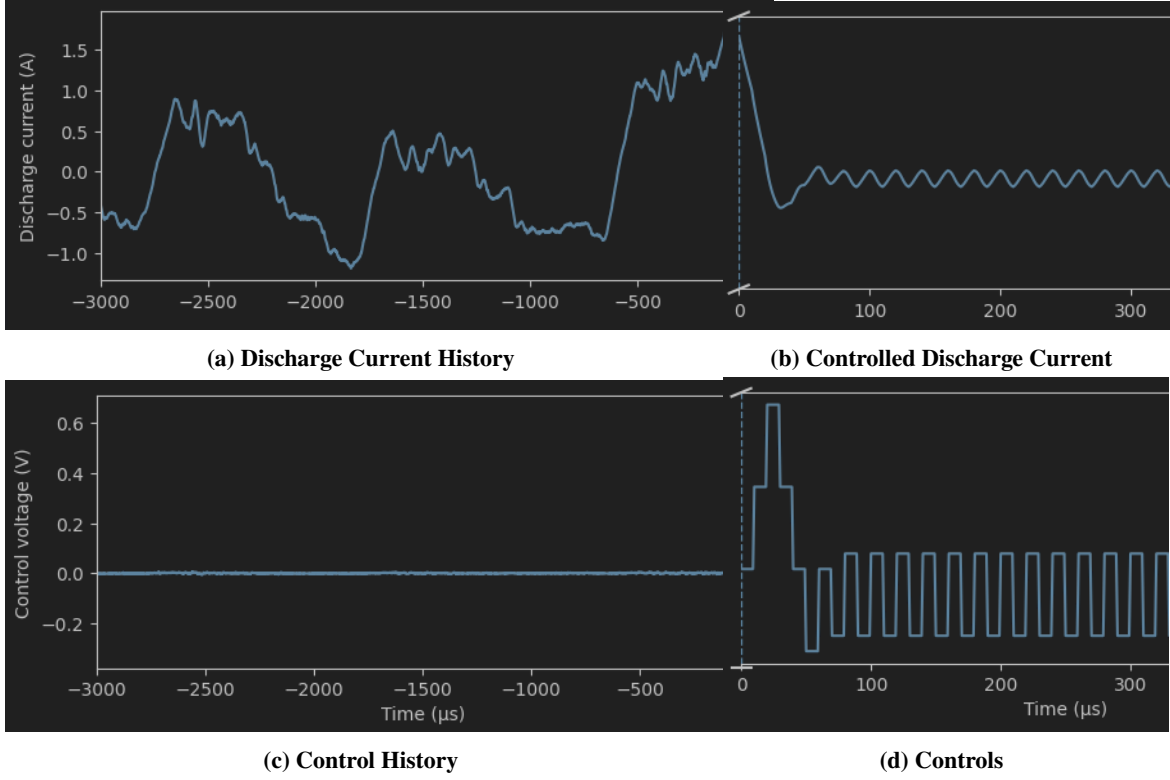


**Fig. 19 PID Control of Discharge Plasma ESN**

### E. ESN Model ML Control Simulation Results

In Figure 20, we see how NMPC affects the discharge current in an ESN simulation, which takes under a minute to complete. We use history of the discharge current at no control to initialize the ESN, and apply NMPC on the ESN to minimize discharge current oscillations. We can see that the oscillations are reduced within  $30 \mu s$  of applying controls. Figure 20d shows the chosen control values at each  $10 \mu s$  step. The PP of the discharge current oscillations reduces from  $3 A_{PP}$  to  $0.2 A_{PP}$ , which is a 93.333% reduction. The control voltage ranges from  $-0.3 V$  to  $0.15 V$ , with zero mean, since the injection path only takes AC signals. Accounting for gains from the amplifiers between the DAC output to the secondaries of the transformers, the perturbation voltage that would arrive at the HET ranges between  $-5.625 V$  and  $2.813 V$ , which is  $8.438 V_{PP}$ . These results show that NMPC on an ESN can be done in simulation and could potentially be used in an experiment. The performance of PID and NMPC in terms of oscillation reduction is comparable, but NMPC requires a lower PP voltage to achieve the same result. NMPC control also acts faster than PID. The results likely will differ in an experiment as simulations do not take into account hardware delays, while repeated updating of the ESN model may reveal superior performance with ML control compared to PID control.

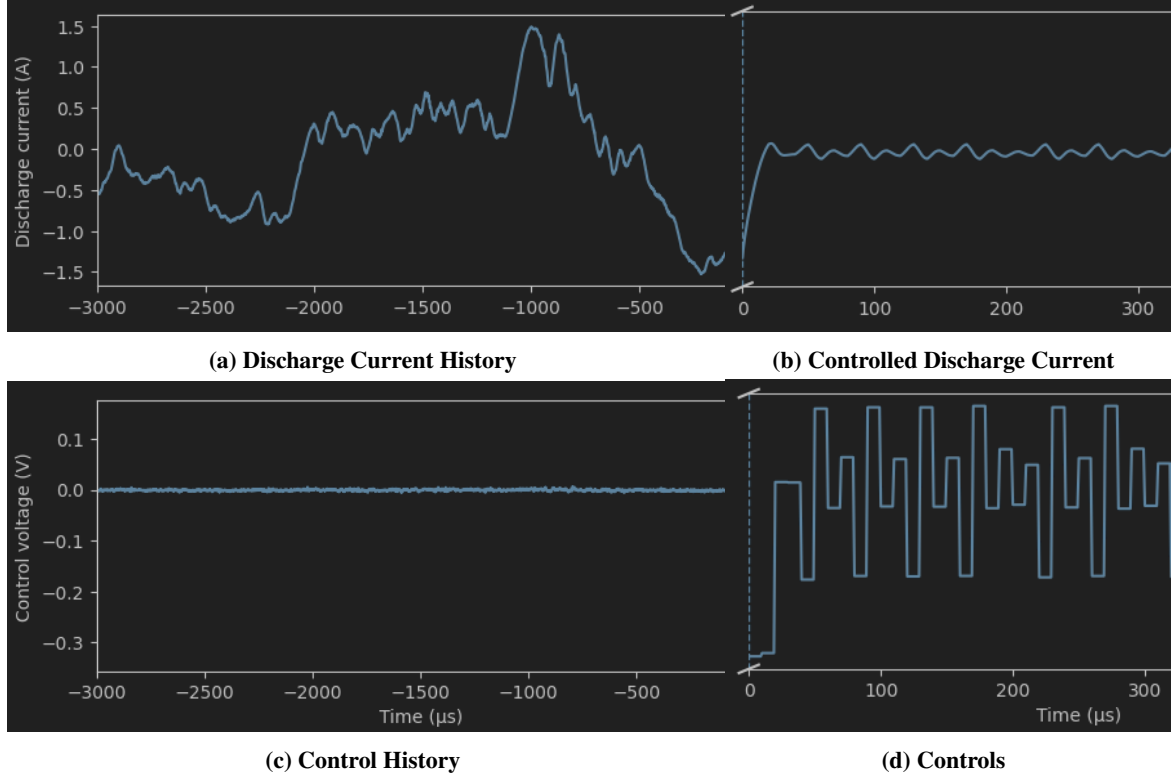


**Fig. 20 NMPC Control of Discharge Plasma ESN**

## VI. ML Control Experiment

Figure 21 shows the ML control experiment setup, where an FPGA is now used rather than a microcontroller for active control. We plan to use the ZCU104 FPGA, the THS1206A ADC, and the DC2459A DAC. These devices are sufficient to enable real-time control using neural networks [39]. The hardware additions could be placed within the PPU itself, but one question to be answered is whether or not the benefits of ML control outweigh the design changes. It is also possible to investigate how ML control affects the plasma using the 0D model along with state estimation using an EKF. Thrust measurements can also be done when phase synchronizing voltage and current oscillations using the ML controller.



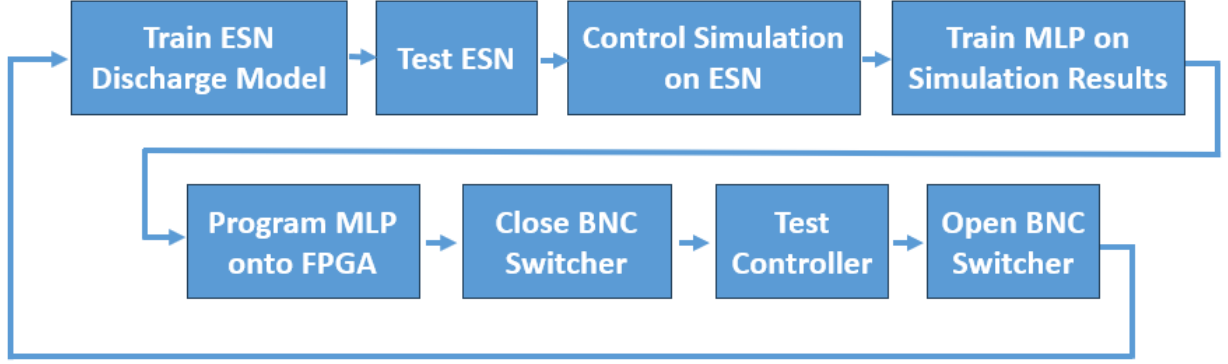


**Fig. 22 ML Control Testing Process**

Analysis would include plasma state estimates with and without ML control, specifically looking into the mean, RMS, and PP of the state estimates. The transient upon activating the control, steady-state, and turning off the control will be analyzed. Breathing mode frequency and amplitude changes will be investigated as well. Lastly, the power draw from using the ML controller will be determined.

## VII. Conclusion

The research described here attempts to create an intelligent power supply that can control HETs in an optimal manner. We demonstrate the ability to control the OD model using PID. We show that perturbations, in the form of PID control, reduce oscillations and impact the discharge current using the eCCM algorithm, revealing reciprocal causality. We use the EKF to determine how plasma parameters change with and without PID control. We demonstrate the effectiveness of ESNs to predict time-resolved discharge current data from a HET by using a diverse dataset of perturbation response data, yielding 90% prediction accuracy by variance. We show that a real-time ML control approach can potentially minimize oscillations through simulation, reducing oscillations by more than 90%. The next step is to demonstrate the controller through an experiment with the hope of demonstrating reduced discharge current oscillations. The ML controller has the potential to work at other operating points, as the same procedure of learning dynamics and computing controls does not change. With advances in rad-hardened GPU and FPGA technology, it has become increasingly possible to employ ML in space missions.

## Appendix

The OD ionization model is derived using the conservation of mass, momentum, and energy equations. It is governed by the following system of eight nonlinear ODEs, which consists of five plasma states ( $N_i, N_n, T_e, U_i, U_e$ ), three electrical states ( $V_{CF}, I_{LH}, V_D$ ), one output ( $I_D$ ), and one control ( $V_M$ ). It is based on Troyetsky's OD model, but contains additions with respect to the RLC harness model and voltage control [11]:

$$\frac{dN_i}{dt} = -\frac{N_i U_i}{L_{ch}} - \frac{2N_i U_{i,w}}{R_\Delta} + N_i N_n \zeta_{ion} \quad (9)$$

$$\frac{dN_n}{dt} = -\frac{(N_n - N_{int})U_n}{L_{ch}} - N_i N_n \zeta_{ion} \quad (10)$$

$$\frac{dT_e}{dt} = \frac{2}{3N_i} (-N_i U_e E - N_i \varepsilon_w v_w - N_i N_n \zeta_{ion} \chi \varepsilon_{ion} - \frac{3}{2} T_e \frac{dN_i}{dt} - \frac{5}{2} \frac{N_i U_e T_e}{L_{ch}}) \quad (11)$$

$$\frac{dU_i}{dt} = \frac{eE}{M_i} + \frac{2U_{i,w}U_i}{R_\Delta} + N_n \zeta_{ion} (U_n - U_i) \quad (12)$$

$$\frac{dU_e}{dt} = 0 \quad (13)$$

$$\frac{dV_{CF}}{dt} = -\frac{I_{LH}}{C_F} + \frac{V_P - V_{CF}}{R_F C_F} \quad (14)$$

$$\frac{dI_{LH}}{dt} = \frac{V_{CF} - V_M - R_H I_{LH} - V_D}{L_H} \quad (15)$$

$$\frac{dV_D}{dt} = \frac{I_{LH}}{C_H} - \frac{e A_C N_i (U_i - U_e)}{C_H} \quad (16)$$

The discharge current is governed by the following relation that links the plasma and electrical circuit differential equations:

$$I_D = e A_C N_i (U_i - U_e) \quad (17)$$

## Acknowledgments

The authors would like to thank all of the undergraduate and graduate student researchers at HPEPL that contributed towards experimental setup and vacuum facility operation, particularly Julian Lopez-Uricoechea, Will Brabston, Nafez Ahmmed, Frank George, Hector Sanchez, Irene Moxley, and Daniel Wochnick. The authors would also like to thank the Georgia Tech Research Corporation for assisting in filing a patent application, US 63/765,398, based on the work presented in this conference paper. Lastly, the authors would like to thank the NASA Joint Advanced Propulsion Institute for its support under the grant number 80NSSC21K1118.

## References

- [1] Brown, D. L., "Investigation of low discharge voltage Hall thruster operating modes and ionization processes," *31st International Electric Propulsion Conference*, Ann Arbor, MI, USA, 2009. IEPC-2009-074.
- [2] Goebel, D., and Katz, I., *Fundamentals of Electric Propulsion: Ion and Hall Thrusters*, Wiley, Hoboken, NJ, 2008.
- [3] Byers, D., "A review of facility effects on Hall effect thrusters," *31st International Electric Propulsion Conference*, Ann Arbor, MI, USA, 2009. IEPC-2009-076.
- [4] Frieman, J. D., "Role of a conducting vacuum chamber in the Hall Effect Thruster Electrical Circuit," *Journal of Propulsion and Power*, 2014.
- [5] Byrne, M. P., "Coupling of electrical and pressure facility effects in Hall effect thruster testing," *37th International Electric Propulsion Conference*, Boston, MA, USA, 2022. IEPC-2022-377.
- [6] Walker, J. A., "Electrical facility effects on hall current thrusters: Electron termination pathway manipulation," *Journal of Propulsion and Power*, 2016.
- [7] Dankanich, J. W., "Recommended practice for pressure measurement and calculation of effective pumping speed in electric propulsion testing," *Journal of Propulsion and Power*, 2017.
- [8] Choueiri, E. Y., "Plasma oscillations in hall thrusters," *Physics of Plasmas*, 2001.
- [9] Fife, J., Martinez-Sanchez, M., Szabo, J., Fife, J., Martinez-Sanchez, M., and Szabo, J., "A numerical study of low-frequency discharge oscillations in Hall thrusters," *33rd Joint Propulsion Conference and Exhibit*, 1997.
- [10] Barral, S., and Ahedo, E., "Theoretical study of the breathing mode in Hall thrusters," *42nd AIAA/ASME/SAE/ASEE Joint Propulsion Conference & Exhibit*, 2006.
- [11] Troyetsky, D. E., Greve, C. M., Tsikata, S., and Hara, K., "State estimation for real-time analysis of dynamic plasma properties and electrical circuit effects in Hall effect thrusters," *37th International Electric Propulsion Conference*, Boston, MA, USA, 2022. IEPC-2022-323.
- [12] Barral, S., "Closed-loop control of ionization oscillations in Hall accelerators," *Physics of Plasmas*, 2011.
- [13] Tamida, T., "Performance Improvement of Hall Thrusters Using a Pulse-Synchronous Driver System," *Journal of Propulsion and Power*, 2015.
- [14] Li, W., "Effect of Low-frequency Oscillation on Performance of Hall Thrusters," *35th International Electric Propulsion Conference*, Atlanta, GA, USA, 2017. IEPC-2017-134.



- [15] Petronio, F., "Study of the breathing mode development in Hall thrusters using hybrid simulations," *Journal of Applied Physics*, 2024.
- [16] Krishnan, A., "Impedance Analysis of the Hall Thruster Discharge Circuit and Plasma Load to Address Harness Facility Effects," *38th International Electric Propulsion Conference*, Toulouse, France, 2024. IEPC-2024-619.
- [17] Ito, K., "Sequential prediction of Hall thruster performance using echo state network models," *Transactions of the Japan Society for Aeronautical and Space Sciences*, 2024.
- [18] Jovel, D. R., "Hall effect thruster impedance characterization in ground-based vacuum test facilities," *Journal of Electric Propulsion*, 2024.
- [19] Thoreau, P., "Rapid thruster-in-the-loop optimization for Hall thrusters," *Journal of Electric Propulsion*, 2025.
- [20] Barral, S., "Numerical investigation of closed-loop control for Hall accelerators," *Journal of Applied Physics*, 2011.
- [21] Wei, L., "Stabilizing Low Frequency Oscillation with Two Stages Filter in Hall Thrusters," *34th International Electric Propulsion Conference*, Shanghai, China, 2015. IEPC-2015-284.
- [22] Brooks, J., "Iterative learning control of the hollow cathode plume mode," *38th International Electric Propulsion Conference*, Toulouse, France, 2024. IEPC-2024-219.
- [23] Simmonds, J., "Studies of a modulated hall thruster," *Plasma Sources Science and Technology*, 2021.
- [24] Slimane, T. B., "Analysis and control of hall effect thruster using optical emission spectroscopy and artificial neural network," *Journal of Applied Physics*, 2024.
- [25] Shaoning, W., "Aerospace Digital and Intelligent Power Supply Technology Research," *FAFEE*, 2024.
- [26] Hopfield, J. J., "Neural networks and physical systems with emergent collective computational abilities," *PNAS*, 1982.
- [27] Sekarak, M. J., "Mode Transitions in Hall Effect Thrusters," *49th AIAA/ASME/SAE/ASEE Joint Propulsion Conference*, Huntsville, AL, USA, 2013. AIAA-2013-4116.
- [28] Piñero, L. R., "The Impact of Harness Impedance on Hall Thruster Discharge Oscillations," *NASA/TM-2017-219722*, 2017.
- [29] Priese, S., "Adaptive feedforward control for active noise cancellation in-ear headphones," *Proceedings of Meetings on Acoustics*, 2012.
- [30] Jorns, B. A., "A Predictive Hall Thruster Model Enabled by Data-Driven Closure," *AIAA Propulsion and Energy Forum*, 2020.
- [31] Armenio, L. B., "Echo State Networks: analysis, training and predictive control," *18th European Control Conference*, Napoli, Italy, 2019.
- [32] Jordanou, J. P., "Echo state networks for practical nonlinear model predictive control of unknown dynamic systems," *IEEE Transactions on Neural Networks and Learning Systems*, 2022.
- [33] Popescu, M.-C., "Multilayer perceptron and neural networks," *WSEAS Transactions on Circuits and Systems*, 2009.
- [34] Kieckhafer, A. W., "Recirculating liquid nitrogen system for operation of cryogenic pumps," *32nd International Electric Propulsion Conference*, Kurhaus, Wiesbaden, Germany, 2011. IEPC-2011-217.
- [35] Wachter, A., "On the implementation of an interior-point filter line-search algorithm for large-scale nonlinear programming," *Mathematical Programming*, 2005.
- [36] Andersson, J. A. E., "CasADi: a software framework for nonlinear optimization and optimal control," *Mathematical Programming Computation*, 2018.
- [37] Huerta, C. E., "Determining causality in hall effect thrusters using extended convergent cross mapping, part I," *Plasma Sources Science and Technology*, 2021.
- [38] Akiba, T., "Optuna: A Next-generation hyperparameter optimization framework," *KDD*, Anchorage, AK, USA, 2019.
- [39] Shi, R., "ML-based Real-Time Control at the Edge: An Approach Using hls4ml," *IEEE International Parallel and Distributed Processing Symposium Workshop*, San Francisco, CA, USA, 2024.

- [40] Paszke, A., "PyTorch: an imperative style, high-performance deep learning library," *Proceedings of the 33rd International Conference on Neural Information Processing Systems*, Vancouver, Canada, 2019.
- [41] Azimi-Sadjadi, M. R., "Fast learning process of multilayer neural networks using recursive least squares method," *IEEE Transactions on Signal Processing*, 1992.
- [42] Hewing, L., "Learning-based model predictive control: toward safe learning in control," *Annual Review of Control, Robotics, and Autonomous Systems*, 2020.